Kinetic Monte Carlo simulation of heteroepitaxial growth: Wetting layers, quantum dots, capping, and nanorings

T. P. Schulze and P. Smereka

Phys. Rev. B **86**, 235313 — Published 26 December 2012

DOI: 10.1103/PhysRevB.86.235313

Kinetic Monte Carlo Simulation of Heteroepitaxial Growth: Wetting Layers, Quantum Dots, Capping, and NanoRings

T.P. Schulze* and P. Smereka†

December 4, 2012

Abstract

A new kinetic Monte Carlo algorithm that efficiently accounts for elastic strain is presented and applied to study various phenomena that take place during heteroepitaxial growth. For example, it is demonstrated that faceted quantum dots occur via the layer-by-layer nucleation of pre-pyramids on top of a critical layer with faceting occurring by anisotropic surface diffusion. It is also shown that the dot growth is enhanced by the depletion of the critical layer which leaves behind a wetting layer. Capping simulations provide insight into the mechanisms behind dot erosion and ring formation. The algorithm used for the simulations presented here is based on the observation that adatom and dimer motion is essentially decoupled from the elastic field. This is exploited by decomposing the film into two parts: the weakly bonded portion and the strongly bonded portion. The weakly bonded portion is taken to evolve independent of the elastic field. In this way the elastic field need only be updated infrequently. Extensive validation reveals that there is little loss of fidelity but the algorithm is fifteen to twenty times faster.

1 Introduction

The simulation of heteroepitaxial growth using kinetic Monte Carlo (KMC) is a promising alternative to continuum formulations such as island dynamics (e.g. Refs. [1, 2, 3]), phase field models (e.g. Refs. [4, 5]), or sharp interface models (e.g. Refs. [6, 7, 8, 9]). The potential benefit of KMC lies in that it can naturally include both discrete and stochastic effects that occur at the nanoscale. Unfortunately, the computational cost incurred by the need to repeatedly update the elastic displacement field makes the use of KMC challenging. However, starting with the work of Lam, Lee, and Sander[10], it became clear that it could be practical to use KMC as a tool to simulate strained epitaxial growth. Since then there have been a number of papers that have improved the state-of-the-art in this area (e.g. Refs. [11, 12, 13, 14, 15, 16]).

In this paper, we present an approach that offers significantly improved computation times for simulating heteroepitaxial growth. Indeed, our simulations are fifteen to twenty times faster than previous ones. Importantly, this has allowed us to access physically relevant parameter regimes in

*Department of Mathematics, University of Tennessee, Knoxville, TN 37996.
†Department of Mathematics, University of Michigan, Ann Arbor, MI 48109.

three dimensions. The new approach takes advantage of a natural separation of length scales that occurs in strained heteroepitaxial growth. Specifically, we use a surface decomposition formulation in which the weakly bonded atoms (e.g. adatoms and dimers) are decoupled from the rest of the film and the associated elastic fields. Before we describe the method further, we wish to emphasize several physical issues the improved method has allowed us to explore.

1.1 Heteroepitaxial Phenomena

To begin, we revisit what is typically referred to as Stranski-Krastanov (SK) growth. This is the scenario normally encountered during strained heteroepitaxial growth, starting off as layer-by-layer, but then suddenly transitioning to island-mode growth after a number of monolayers have been deposited. For example, when depositing InAs on GaAs it is observed that three dimensional dots form after 1.5 ML of deposition [17]. This suggests some sort of instability has occurred; however, the issue is rather more complicated than that. The early work of Asaro & Tiller [18] and Grinfeld [19] reveals a critical thickness of zero—all strained films are unstable irrespective of their thickness. This, in turn, lead Spencer, Voorhees and Davis [8] to suggest that the critical thickness observed in experiments is an "apparent critical thickness," the suggestion being instability is there at all thicknesses, but is not readily observed until it reaches a certain stage of development. An alternative explanation originated with the work of Tersoff [20]. Based on calculations using intermolecular potentials, he argued that up to three layers of Ge would be stable on Si. This led to models with wetting potentials, e.g. Ref. [7], with a specified critical thicknesses "hard-wired" into the form of the potential. More recently, Baskaran and Smereka [21], have used a 1+1 dimensional KMC theory to show that there is indeed a critical thickness, but that subsequent growth of the islands actually leads to a depletion of the original critical layer, leaving behind what we will refer to as a wetting layer.

Although kinetic Monte Carlo models in 1+1 dimensions (e.g. [10, 21, 22, 23, 24, 25]) offer much insight into strained epitaxial growth, they cannot be considered definitive, as there are significant differences between the behavior of atomistic models in 2+1 and 1+1 dimensions. For example, in equilibrium it is known that a one dimensional surface cannot have true facets, whereas two dimensional surfaces can form facets below the roughening temperature (e.g. [26], p. 60). This is also reflected by the fact that the equilibrium shape of an island for a bond counting model is convex in two dimensions [27, 28] but not so in three dimensions [29]. Other differences between two and three dimensions are discussed by Leamy, Gilmer, and Jackson [30]. These differences can be hidden in the context of continuum models. For example, the Wulff shape can be arbitrarily specified to give facets irrespective of dimension.

With this discussion in mind, our first aim here is to closely examine the emergence of faceted islands—quantum dots. Again, this issue is especially confusing and cannot be completely understood from a continuum perspective. The very existence of a wetting layer indicates that the initial growth direction should be a facet, and as such it should be very difficult to change this growth direction since "nearby" directions have much greater surface energies (e.g. [34]). Often, continuum models have dealt with this issue by modifying the surface energy to induce the growth of new facets [43, 6]. While this gives the correct growth shapes, it cannot offer a mechanism by which this happens. Our KMC simulations suggest, in agreement with the prediction of Xiang *et al.* [31], that the mechanism is the layer-by-layer nucleation of a pre-pyramid which then evolves into a fully faceted pyramid by anisotropic surface diffusion. By "pre-pryamid" we mean a small multilayer three dimensional island whose sides are not faceted. Pre-pryamids can be either circular or irregular in shape.

We next turn to the topic of capping of the quantum dots with additional layers of the substrate material. Our KMC simulations show that the capping procedure can lead to significant erosion of the quantum dots, in agreement with experimental observations. In addition the simulations reveal a possible mechanism for this erosion: it is energetically favorable for the wetting layer to be composed of dot material, therefore as the capping proceeds dot material is driven from dots onto the wetting layer by capillary-like forces. Our simulations can also reproduce a particularly striking result: the act of capping can produce ring-shaped dots. This result seems to indicate that ring formation is the result of strain relaxation. Finally, our simulations provide some new insight into the mechanisms that lead to the alignment of stacked quantum dots.

1.2 Computational Framework

Our method is based on the observation that adatoms and dimers are weakly coupled to the elastic field. Several tests reveal that this is an excellent assumption which also sheds light on aspects of heteroepitaxial growth. For example, our calculations show that the mechanism involved in the stacking of quantum dots involves a collective phenomena and is not the result of enhanced nucleation in the region above the buried dot.

To get at the issues outlined above, we needed to introduce further modifications to our earlier methods aimed at improving computational speed [15, 16]. Our goal is to perform simulations on length scales close to one hundred nanometers and time scales of tens of seconds in physically realistic parameter regimes. Unfortunately, simulating epitaxial systems with strain is orders of magnitude more expensive than simulating systems without strain because the elastic displacement field is nonlocal and often sensitive to atomistic scale detail. As a result, the bulk of KMC simulations of heteroepitaxial growth have implemented some form of elastic update after each atomistic event. Much of the recent effort in this area has focussed on efficient algorithms for computing this displacement field using a combination of both local and global updates [13, 14, 15, 16, 22]. Even with the techniques and approximations introduced in these earlier works, to complete the sort of computations we are striving for it would take something like year on a typical single core machine (e.g. Intel Xeon 5650, 2.66 GHz).

To achieve our goals, the current simulations exploit a separation of scales based on the local coordination of surface atoms. More specifically, the surface of the film is partitioned into two nonoverlapping regions, $S = S_w \cup S_s$, according to how strongly individual atoms are bonded to the surface.

Following the work of Burton, Cabrerra and Frank (BCF) [32], there has been a long tradition in the epitaxial growth literature of partitioning the film surface into a height profile, $h(x)$, and an "adatom" density, $\rho(x)$, of uncoordinated surface atoms. This recognizes the fact that, to a good approximation, these atoms diffuse independently on the surface of the film. This idea has been extended to heteroepitaxial growth, and used to perform simulations using the island dynamics formulation of a BCF-like model [1, 2, 3]. The approximation we have in mind is inspired by these simulations. A key observation made by these investigators is that it should not really be necessary to update the elastic displacement field based on the motion of individual adatoms. In the case of island dynamics, this observation is very naturally incorporated since an implicit time stepping strategy is employed when updating the adatom field. In this way, many adatoms will attach or detach from the island boundary before the elastic field is updated.

Within the KMC literature, which aims for a more resolved atomistic view of the film surface, the adatom concept has also occasionally found uses, as the motion of adatoms invariably dominates the computational cost of KMC simulations. In Ref. [33], for example, the surface of the film is

partitioned into regions surrounding steps, where KMC simulations are performed, and "vicinal" regions, where diffusion equations conserve the flux of adatoms to the steps. Adatom motion is treated using a "big-hop" approximation in Ref. [28]. More recently, in Ref. [16] it was observed that the influence of the elastic field on the rates of adatoms was relatively weak, and that adatoms had a correspondingly weak influence on the elastic field of neighboring sites. Thus, omitting the elastic computations for adatom motion is both highly efficient, due to the dominance of these events, and reasonably accurate. This latter study again relied on a version of the big-hop approximation that, while effective, proved somewhat difficult to implement. Here, we adopt an alternative approach, based on the domain decomposition mentioned above, that offers both a streamlined implementation and is readily extended to include any sort of weakly bonded atom. The result is surprisingly effective, yielding simulations that are fifteen to twenty times faster while retaining a high degree of accuracy.

In the next section, we review the model and previous numerical approximations of this model before continuing with the present approach.

2 KMC Model

Like most KMC models, we assume a Markov chain dynamics that has the system making transitions between states that consist of nearest neighbor single-atom moves on the surface.

2.1 General Considerations

In an off-lattice KMC, based on transition state theory and an empirical potential or perhaps even a density functional theory, one would compute hopping rates between states w and w' as

$$r_{w\to w'} = K \exp\left[-E_B/kT\right],$$

where k is Boltzmann's constant, T is the temperature of the film, and $1/K$ is a time scale determined by details of the crystal, typically $K = 10^{12}$ to 10^{13} sec^{-1}, and $E_B = E_T - E_W$ is the energy needed to rise out of a local minimum of the potential with energy E_W, cross a transition/saddle point with energy E_T, and escape to a neighboring local energy well. It is easy to show that these models satisfy detailed balance.

In a lattice-based model without elastic effects, the energy is only defined for lattice configurations, and the energy barrier E_B is often taken to be linear in the number and types of bonds to adjacent lattice sites. If one defines an Ising model potential,

$$U = -N\varepsilon,$$

based on a similar bond-counting scheme with N the total number of bonds in the system and ε a bond energy, then one can see that such bond-counting models for the rates are equivalent to the following:

$$E_B = -\Delta U, \qquad \text{where}$$

$$\Delta U = U(\text{with surface atom } (i,j)) - U(\text{without surface atom } (i,j)). \tag{1}$$

In equilibrium, the probability of being in state w is

$$\rho_w = C \exp(-U(w)/kT),$$

where C is a normalization constant. Detailed balance requires

$$r_{w\to w'}\rho_w = r_{w'\to w}\rho_{w'}.$$

The bond-counting model for the rates in the form (1) is readily seen to satisfy this relationship.

Notice that the term $U(\text{without surface atom}(i,j))$ is playing the role of the transition-state energy. It is important that this quantity is the same between any pair of communicating states. By defining the "transition state" in this way, this condition is automatically satisfied, as the "atom off" state is the same for both the original configuration and the destination regardless of which way the transition takes place.

In reality $-\Delta U$ is a fairly poor approximation to E_B. To gain additional flexibility in the model without altering the detailed balance relationship, we can modify this to $E_B = -(U_0 + \Delta U)$. This is the most commonly used model in the KMC literature.

The type of model that we consider in this paper was proposed by Orr *et al.* [25] and has been extended by a number of different investigators (e.g. [10, 12, 14, 15, 22]). In short, this is a cube-on-cube, bond counting model that has been modified to include elastic effects. The state of the system is described by a discrete height array h_{ij}, supplemented by a discrete displacement field, $\mathbf{u}_{ijk}$. Associated with each of these is a potential energy—the former corresponding to an Ising type potential U, the latter a discrete elastic energy W. We assume these quantities add to give the total energy of the system $E = U + W$. This model is capable of capturing many qualitative aspects of heterepitaxial growth. It is, however, still limited in that it uses a simple cubic lattice and cannot account for crystal defects, e.g. dislocations.

In a fashion similar to the bond-counting model (1), the transitions occur with rates that only depend on the initial state and the location of the hopping particle:

$$r_{ij} = K \exp\left[(E_0 + \Delta E)/k_B T\right], \tag{2}$$

where $\{ij\}$ indicates the initial position of the atom making the move and $-(E_0+\Delta E)$ is the energy barrier that must be overcome in making the transition. As with U_0 above, we take E_0 as a fixed constant and

$$\Delta E = E(\text{with surface atom } (i,j)) - E(\text{without surface atom } (i,j)). \tag{3}$$

Like the energy, ΔE now consists of two pieces: one that depends only on h_{ij} and that is of the type found in bond-counting schemes without elastic effects and one that depends only on the elastic energy,

$$\Delta E = \Delta U + \Delta W.$$

Finally, W is the total elastic contribution to the energy and, in analogy with (1), we have

$$\Delta W = W(\text{with surface atom } (i,j)) - W(\text{without surface atom } (i,j)). \tag{4}$$

The rates given by (2) also satisfy detail balance.

2.2 Model Parameters

As described in Ref. [16], we shall consider two species of atoms denoted type 1 and type 2. For most of our simulations we will consider the situation in which atoms of type 2 are deposited on a substrate of type 1. We will let $\gamma_{\alpha\beta}$ denote the bond strength between atoms of type α and type β. For this model, ΔU for a surface atom at site (i,j) is given by

$$\Delta U = -(B_{11} + B_{22} + B_{12}), \tag{5}$$

with

$$B_{\alpha\beta} = \left(aN_{\alpha\beta}^{(1)} + bN_{\alpha\beta}^{(2)} + cN_{\alpha\beta}^{(3)} \right) \gamma_{\alpha\beta}, \tag{6}$$

where $\gamma_{\alpha\beta}$ is strength of the interaction, $N_{\alpha,\beta}^{(1)}$ denotes the total number of bonds of type α and β connecting the atom at site (i, j) and its nearest neighbors, $N_{\alpha\beta}^{(2)}$ and $N_{\alpha\beta}^{(3)}$ are analogously defined but for next nearest neighbors and next to next nearest neighbors respectively. We choose

$$E_0 = -E_D + (a + 4b + 4c)\gamma_{12}.$$

This implies that E_D is the energy barrier for the diffusion of a type 2 adatom on a type 1 substrate (ignoring the ΔW term for now). We point out that more sophisticated bond counting models have been proposed in Refs. [23, 24] in the context of heteroepitaxy.

The parameters a, b, and c allow one vary the anisotropy of the crystal. For example, the surface energy per unit area for (100) facet of material 1 is

$$\sigma_{001} = \frac{(a + 4b + 4c)\gamma_{11}}{2\ell^2}, \tag{7}$$

where ℓ is the size of the cubic unit cell. In addition the surface energy per unit area for the (011) and (111) facets are, respectively, given by

$$\sigma_{011} = \frac{(2a + 6b + 4c)\gamma_{11}}{2\ell^2\sqrt{2}} \tag{8}$$

and

$$\sigma_{111} = \frac{(3a + 6b + 5c)\gamma_{11}}{2\ell^2\sqrt{3}}. \tag{9}$$

These expressions are computed by counting the number of broken bonds. The values σ_{001} and σ_{011} can be found in the book by Markov [34].

The elastic interactions are accounted for by using a ball and spring model with longitudinal and diagonal springs having spring constants k_L and k_D respectively. The elastic effects arise because the natural bond length of materials 1 and 2 are different. We will denote these lengths as a_1 and a_2. The misfit is then $\mu = (a_2 - a_1)/a_1$. The details of this model can be found in Russo and Smereka [14] and Baskaran *et al.* [22]. For this model, if one has a flat film of material 2 on a substrate of material 1 then the elastic energy per bulk atom in the film is

$$w_{film} = \frac{4k_D^2 + 5k_Lk_D + k_L^2}{k_L + 2k_D}\mu^2.$$

The spring constants will be estimated by using the continuum limit of the ball and spring model. For the single species case, the energy per atom can be written as

$$w_{atom} = (\ell^2/2)\left[(k_L + 2k_D)(e_{11}^2 + e_{22}^2 + e_{33}^2) + 2k_D(e_{11}e_{22} + e_{11}e_{33} + e_{22}e_{33}) + 4k_D(e_{12}^2 + e_{13}^2 + e_{23}^2)\right],$$

where e_{ij} is the strain tensor. The energy density per unit volume is then $w = w_{atom}/\ell^3$. Therefore we can write

$$w = \frac{1}{2}C_{11}(e_{11}^2 + e_{22}^2 + e_{33}^2) + C_{12}(e_{11}e_{22} + e_{11}e_{33} + e_{22}e_{33}) + 2C_{44}(e_{12}^2 + e_{13}^2 + e_{23}^2),$$

where

$$C_{11} = (k_L + 2k_D)/\ell, \quad C_{12} = k_D/\ell, \quad \text{and} \quad C_{44} = k_D/\ell. \tag{10}$$

The above formulas will be used later in the paper.

3 KMC Implementation

In this section, we start by reviewing the Local Energy Method which was introduced in Ref. [16]. While this was a significant advance, allowing the computation of three-dimensional films on scales previously unreachable, we were unable to access physically realistic parameter regimes which have lower deposition rates and larger islands than we were able to compute with that method. In Section 3.2, we gain another leap in computational performance through the use of a surface decomposition technique, allowing us to access physically realistic regimes. The rest of the section is spent validating the method by comparing to the results of the previous method.

3.1 Local Energy Method

It is specifically the computation of ΔW (Eq. 4) that makes these simulations so much more costly than simulations that involve only a bond-counting formula, as each rate requires one to solve a linear system, and, in principal, one needs to update the hopping rate of all of the surface atoms after each event. In Ref. [16], an approximation is introduced that goes a long way toward mitigating this problem. It is observed that ΔW is close to being proportional to the energy in the springs immediately adjacent to the atom whose rate is being calculated; in other words

$$\Delta W = C w_{ij}, \tag{11}$$

where w_{ij} is the energy in the springs connected to the surface atom at site (i, j) and C depends only on the ratio of the spring constants k_L and k_D. For example, if $k_L = 2k_D$ then $C = 1.33$ and if $k_D = (10/3)k_L$, $C = 1.5$ (see Figure 1 of Ref. [16] for the first case).

While this is not an exact relationship, arguments based on continuum elasticity suggest the error is small, and careful comparison with simulations not using this approximation support this assertion, which has the added advantage of being relatively easy to explain and implement, so we will use this approach in all of the calculations presented in this paper. We refer to this as the Local Energy Method. This approximation is similar to that used in Ref. [3]. For a procedure somewhat more faithful to the model introduced above, an alternative would be to use the techniques introduced in Ref. [15].

With this approximation in place, only a single linear system need be solved per event. Even this is a large numerical task when compared to the local update that accompanies an event in a simple, bond-counting KMC simulation. Ultimately, we will deal with these calculations in one of three ways. Moves of low-coordinated atoms will use rates that depend only on the bond counting part, as we will demonstrate that the elastic contribution is negligible. For the highly-coordinated atoms, we will mostly rely on a locally constrained calculation, where the displacement field beyond a certain distance from the move is held fixed and serves as a boundary condition for the local update. We have used these local updates in our earlier work, developing an efficient numerical procedure, the Expanding Box Method, to perform these calculations [15, 22]. Similar ideas have been used in off-lattice simulations [35, 36], where this is typically referred to as a "frozen crystal" approximation. The local calculations leave small residual forces at the boundaries, which accumulate over the course of the calculation, and must occasionally be relaxed by performing a full, global solution of the system. The latter calculations use an artificial far-field boundary condition with a multigrid procedure for solving the linear system [13, 14].

3.2 Surface Decomposition KMC

The new technique being introduced in this paper is to decompose the surface into two subsets, one for highly coordinated sites and one for low coordinated sites. Effectively, one has

$$h_{ij} = \bar{h}_{ij} + \Delta h_{ij},$$

where $\bar{h}_{ij}$ is the profile of the film with the weakly bonded atoms removed. For the low-coordinated sites, the bond-counting term, U, dominates, while both U and W (the elastic energy) are important for the highly-coordinates sites. This can be seen by examining Figures 1 and 2. Figure 1 demonstrates how the variation in the elastic energy density is largely confined to the boundary of islands and is not significantly affected by the removal of the adatoms and dimers from the surface. Figure 2 shows close-ups of the same calculations shown in Figure 1, but zoomed into the lower left quarter of the images in Figure 1. This view reveals important details, described below, of the elastic density field in the vicinity of adatoms and vacancies that are not readily apparent in the first view.

In the upper left panel of Figures 1 and 2, we have a typical surface configuration, showing two quantum dots with many adatoms. The dots are resting on one monolayer of material 2 which, in turn, is on an infinitely deep substrate of material 1. It is important to note there are several vacancies in the monolayer of material 2. In the panel below this, we plot the local elastic energy, w_{ij}: the sum of the energy in the springs connected to the surface atom at site (i, j). One observes that this quantity is large around the rim of islands, where it would increase the hopping rate, and that it is almost zero for both adatoms and vacancies that penetrate to the substrate. More careful observations reveal that not only is the local elastic energy of the adatoms small, but, unlike the vacancies, the adatoms do little to disturb their environment. This turns out to be true of all low coordinated sites, and is easy to understand in terms of the ball-and-spring model—there simply is not much constraining a low-coordinated atom, so the springs can relax almost completely.

In the upper right panels of Figures 1 and 2, these low-coordinated atoms have been removed from the surface, and the resulting local elastic energy is plotted directly below in the lower right panels. Notice that this has had little effect on the regions where the local elastic energy is large—the rims of the islands. Further, it replaces the local elastic energy at the locations where low-coordinated atoms have been removed with a local elastic energy that fits smoothly into its environment. This is important because it means that these values can be used to get a realistic hopping rate once the low-coordinated atom has moved off of the site without having to update the elastic field.

3.2.1 Detailed balance

The total energy of the system using the Surface Decomposition Method is approximated by

$$\widetilde{E} = U + \overline{W},$$

where U is the bond-counting energy defined earlier and $\overline{W}$ is the elastic energy corresponding to the profile $\bar{h}$. When $\widetilde{E}$ is used in place of E in Eq. (2) the rates will still satisfy detailed balance, which can be seen as follows. As with the earlier model, the "atom off" state can readily be seen to give the same energy for any two states that are connected by an allowed transition, and this, once again, mimics the role of the transition-state energy, ensuring that detailed balance is satisfied.

3.2.2 Algorithm

1. Initialization

   (a) Determine ΔU for every surface atom by bound counting.

   (b) Determine the denuded configuration $\bar{h}$ by removing any surface atom with coordination $N \leq N_C = 6$.

   (c) Perform a global elastic solve for the configuration $\bar{h}$, computing $\Delta W = C\bar{w}_{ij}$ for every surface atom of the denuded configuration.

   (d) The rates for surface atoms of the actual configuration h are then initialized to

$$r_{ij} = \begin{cases} K' \exp(\Delta U/kT) & \text{if} \quad N_{ij} \leq N_c, \\ K' \exp(\Delta U/kT + \Delta W/kT) & \text{if} \quad N_{ij} > N_c, \end{cases}$$

   where $K' = Ke^{E_0/kT}$, ΔU is given by Eq. (5), and ΔW is given by Eq. (11).

2. Select an event by choosing a uniformly distributed random number $r \in [0, R)$, with $R = r_{dep} + \sum r_{ij}$. The event to which r corresponds is located using a binary tree search [37].

3. If the event selected is a deposition, a site is selected at random and an atom is added there; otherwise the event is a hop and the selected atom is moved to one of the four lateral neighbor sites selected at random.

4. The values of ΔU_{ij} are updated as needed.

5. If the denuded configuration is changed then one performs a local elastic solve using an expanding box of size S centered at the site of the selected atom.

6. Every $N_G = 10^5$ steps, update the entire displacement field of the denuded configuration. The results are quite insensitive to the choice of N_G; for example changing N_G to 10^6 gives similar results for all the cases presented in this paper.

7. Repeat steps 2 through 6.

3.3 Verification

It turns out that the new approach is fast enough that one can get much closer to simulating physically relevant systems. However, we wish to compare with our old approach [16] in order to establish the validity of the new formulation, which is now roughly fifteen times faster. This comparison is not feasible using physically relevant parameters, so we choose more convenient parameters for this purpose.

Roughly speaking the surface energies are on the low side for semiconductor materials, while the spring constants are on the high side, but this allows us to observe island formation on time and length scales accessible to our previous code.

In this section we take

$$a = 0.3,\ b = 0.5,\ c = 1,\ \gamma_{11} = 0.26\,\text{eV},\ \gamma_{12} = 0.2425\,\text{eV}, \quad \text{and} \quad \gamma_{22} = 0.225\,\text{eV}.$$

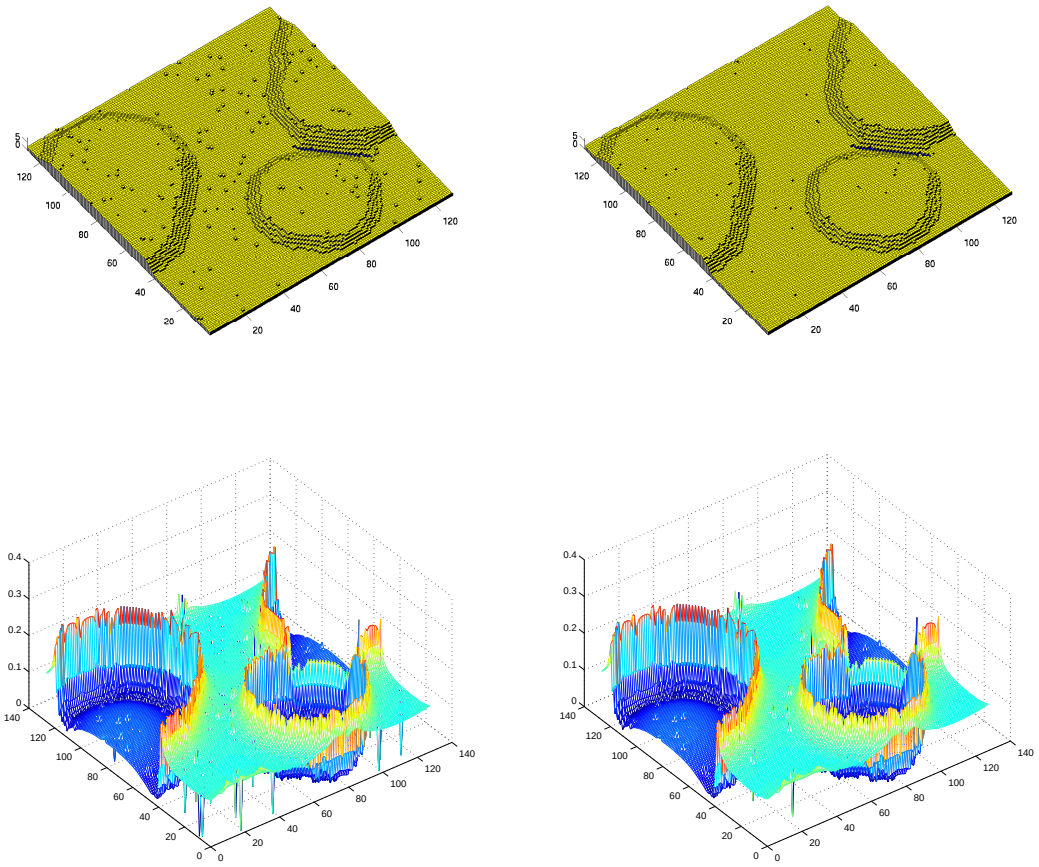

Figure 1: The upper panels show surface configurations with and without low coordinated atoms, whereas the lower panels show the respective elastic energy densities (w_{ij}). Notice that the elastic energy is low on the tops of the islands because the film is relaxed compared to the single monolayer of coverage on the rest of the surface. Also, notice that the largest concentration of energy density is on the boundary of the islands. Recall w_{ij} is the sum of the energy in the springs connected to the surface atom at site (i, j).

If one takes $\ell = 2.7$ Å, then using Eqs. (7 - 9), for material 1 we find the following surface energies for the indicated facets:

$$\sigma_{100} = 1800\,\mathrm{erg/cm^2}, \qquad \sigma_{110} = 1535\,\mathrm{erg/cm^2} \quad \text{and} \quad \sigma_{111} = 1468\,\mathrm{erg/cm^2}.$$

In addition, we take $\mu = .05$, $k_L = 15\mathrm{eV}/\ell^2$ and $k_D = 7.5\mathrm{eV}/\ell^2$, which, using Eq. 10, corresponds to

$$C_{11} = 30\mathrm{eV}/\ell^3 \quad \text{and} \quad C_{12} = C_{44} = 7.5\mathrm{eV}/\ell^3,$$

or

$$C_{11} = 24.42 \times 10^{11}\,\mathrm{dynes/cm^2} \quad \text{and} \quad C_{12} = C_{44} = 6.104 \times 10^{11}\,\mathrm{dynes/cm^2}.$$

We take $E_D = 0.8\,\mathrm{eV}$, $K = 10^{12}\,\mathrm{sec}^{-1}$, and $T = 700$ K.

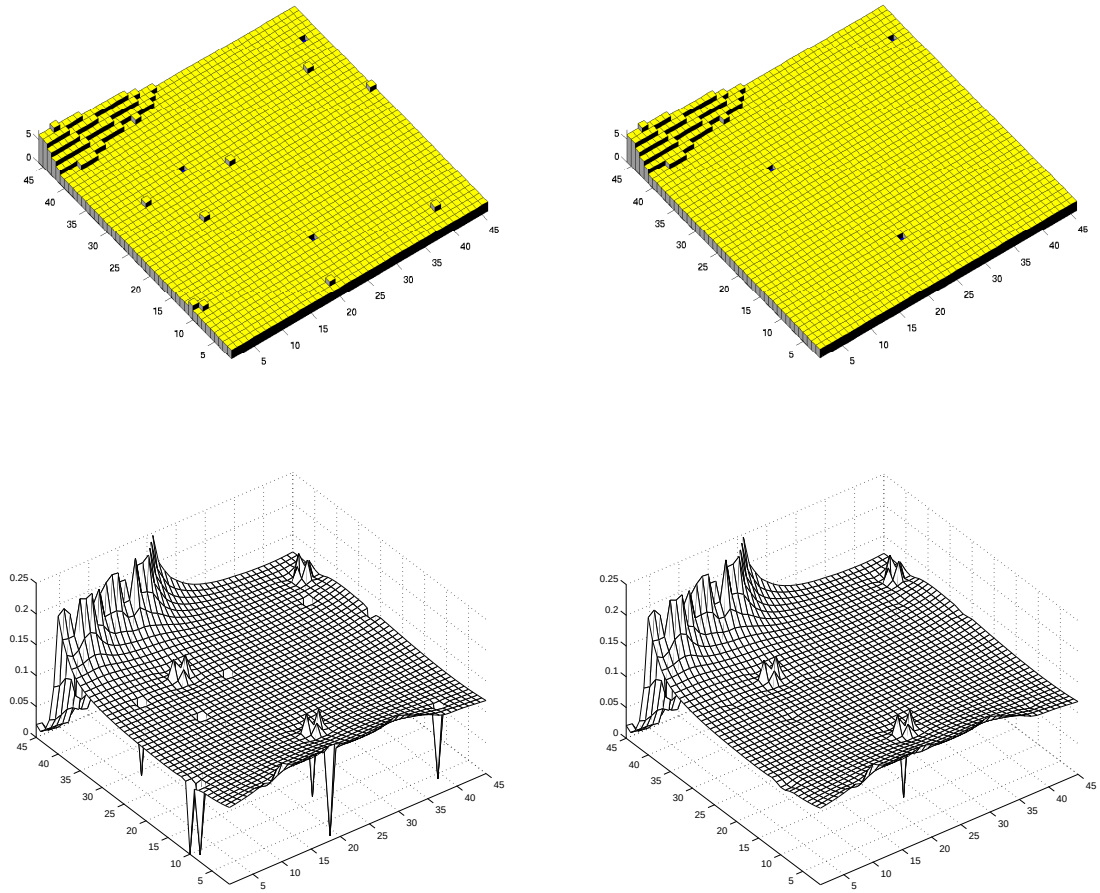

Figure 2: This is the same as figure 1 except each panel is zoomed in to the lower right corner. This allows one to see individual adatom and vacancies. Notice that removal of adatoms has little affect on the surrounding energy density.

3.3.1 Submonolayer Growth

In our first test, we consider the deposition of 0.2 ML, at a rate of 0.5 ML/sec, of material 2 on a substrate composed of material 1. The lattice is 512×512, which corresponds to roughly 138 nm $\times$ 138 nm. We compute the island size distribution for an ensemble with ten realizations using both the Surface Decomposition Method and the Local Energy Method. The results are presented in Figure 3 and show good agreement. In addition, for further comparison, we present the island size distribution when elastic interactions are ignored. This shows that the effect of elastic interactions is to both narrow the size distribution and reduce the average size of the islands. This is in agreement with the island dynamics simulation of Ratsch *et al.* [3].

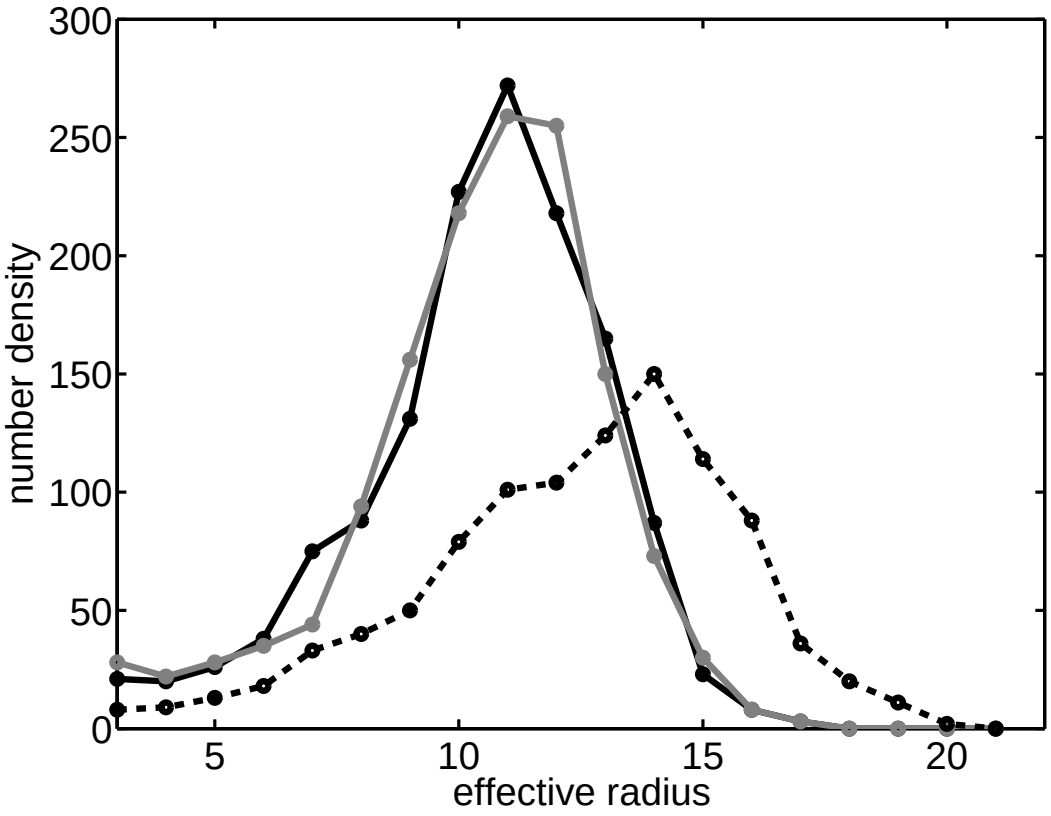

Figure 3: Island size distributions for the Local Energy Method (grey line), Surface Decomposition Method (black line), and with no elastic effects (dashed black line).

3.3.2 Three Dimensional Islands

Here we consider multilayer growth of material 2 on material 1 using a substrate of size 128×128. The deposition rate is 1 ML/sec. In this simulation we see the formation of a wettng layer with subsequent growth of three dimensional islands. Our basic tool for comparing results of different simulations is a radially averaged autocorrelation function. First, we define $\tilde{h} = h - \langle h \rangle$, where $\langle h \rangle$ is the mean surface height and compute the discrete form of

$$I(u,v) = \int \int \tilde{h}(x-u, y-v)\tilde{h}(x,y)\, dxdy,$$

followed by

$$g(R) = \frac{1}{2\pi R} \int \int I\left(u(r,\theta), v(r,\theta)\right) \delta_a(r-R)\, drd\theta,$$

where δ_a is a mollified delta function. This gives a fairly robust measure of film characteristics at different length scales.

The results are summarized in Figure 4 which shows the ensemble average of 10 autocorrelation functions for each method. The figure shows that both methods produce autocorrelation functions that are in good agreement with each other. There is one slight difference, however. It seems that

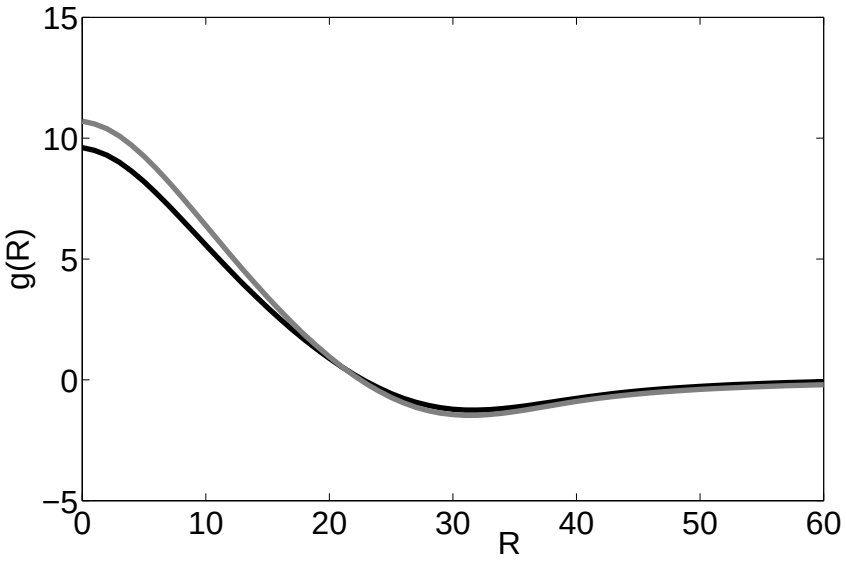

Figure 4: The black and grey curves are the ensemble averaged auto correlation function for the Surface Decomposition Method and the Local Energy Method, respectively. Ten simulations were used for each ensemble.

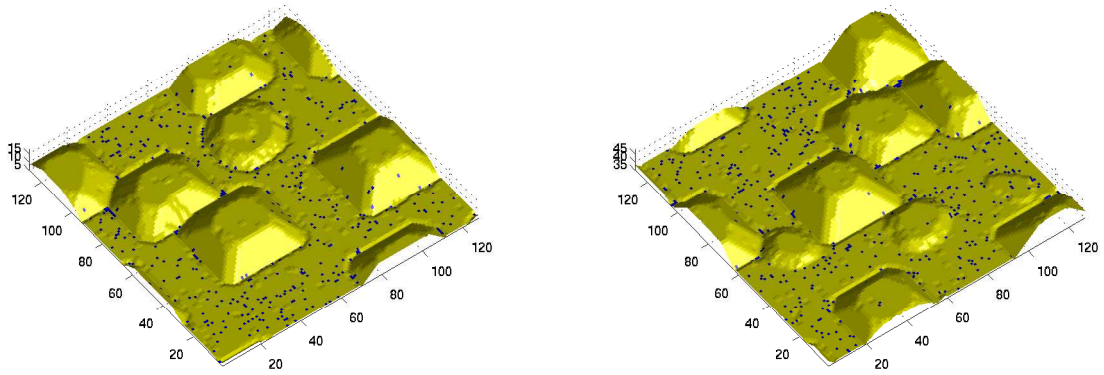

Figure 5: Three dimensional island formation after three monolayers of deposition computed using both the Local Energy Method and the Surface Decomposition Method. The qualitative similarity reinforces the detailed statistics presented in Figures 3 and 4.

the Local Energy Method produces results that are slightly rougher than the Surface Decomposition Method. Figure 5 shows two simulations after three monolayers of deposition, one with each of the two methods. The qualitative similarity of the two surfaces reflects the agreement seen in the data presented in Figures 3 and 4.

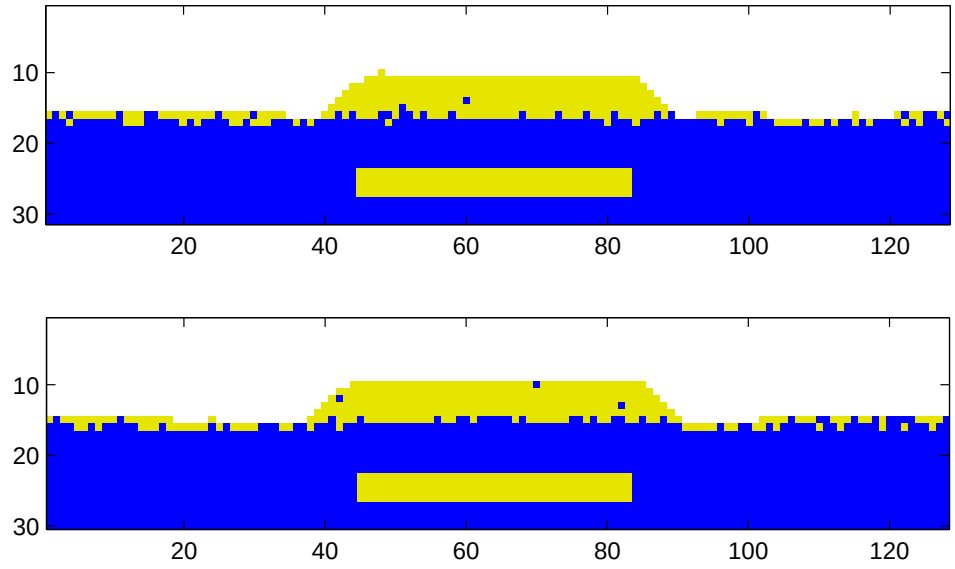

Figure 6: Cross sections after 1.4 monolayers of deposition. The upper figure results from using the Local Energy Method, while the lower one uses the Surface Decomposition Method.

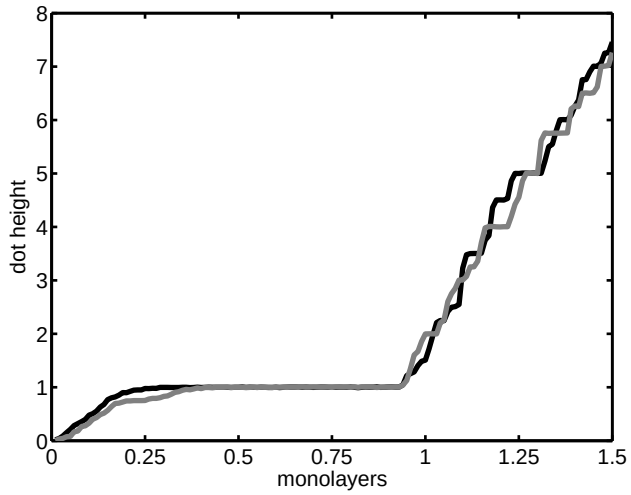

Figure 7: Dot height as a function of the number of deposited monolayers. The Surface Decomposition Method is plotted in black, whereas the Local Energy Method is plotted in grey.

3.3.3 Quantum Dot Alignment

In this test, we consider the situation in which a cylindrical region of material 2 is buried in the center of a substrate of material 1, henceforth referred to as a buried dot. For this test case, g_{12} was changed to 0.23 to suppress the amount of intermixing. Material 2 is then deposited on to the substrate at a rate of 0.1 ML/sec. Due to the presence of the buried dot it is energetically preferred

for a three dimensional island to form directly above the buried dot. Indeed this is exactly what happens. Figure 6 shows a cross section of our system after 1.4 ML of deposition. One can clearly see the three dimensional island has aligned itself with the buried dot for both approaches. To assess whether or not the dynamics of both approaches agree, we consider the following quantity referred to as the dot height:

$$h_{dot} = \frac{1}{\pi R^2} \int \int_{|\boldsymbol{x}-\boldsymbol{x}_c|<R} h(x,y)\, dxdy,$$

which is the average height in a local region centered over the buried dot. In the above formula $\boldsymbol{x} = (x,y)^T$ and $\boldsymbol{x}_c$ is the horizontal location of the center of the buried dot. Figure 7 shows a plot of the ensemble averaged island height as function of the amount of material deposited for both methods with $R = 10$. The agreement is quite good.

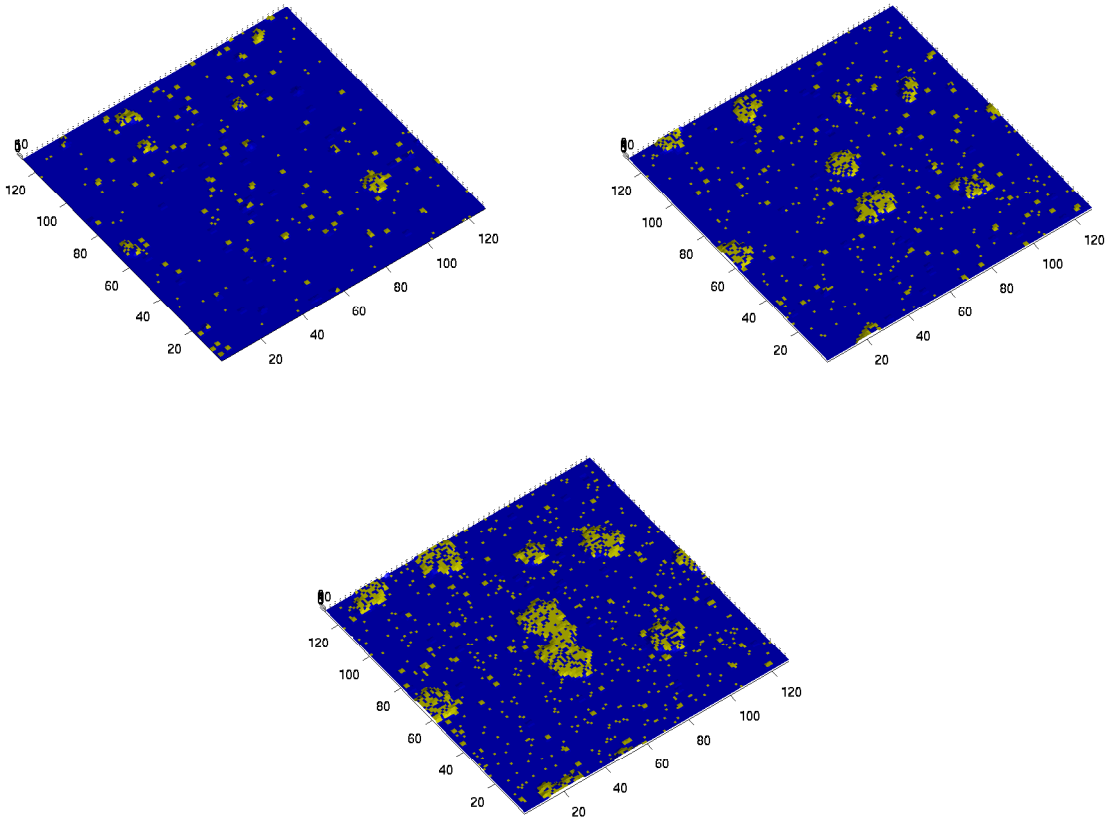

Figure 8: Results after a very small amount of deposition. From left to right and top to bottom the amount of material deposited is .02 ML, .05ML and .1 ML, respectively. The buried dot is centered in the middle of the substrate. A cross section showing the buried dot is displayed in Figure 6. This figure shows that the islands must become sufficiently large before their elastic interaction with the buried dot is strong enough to result in alignment.

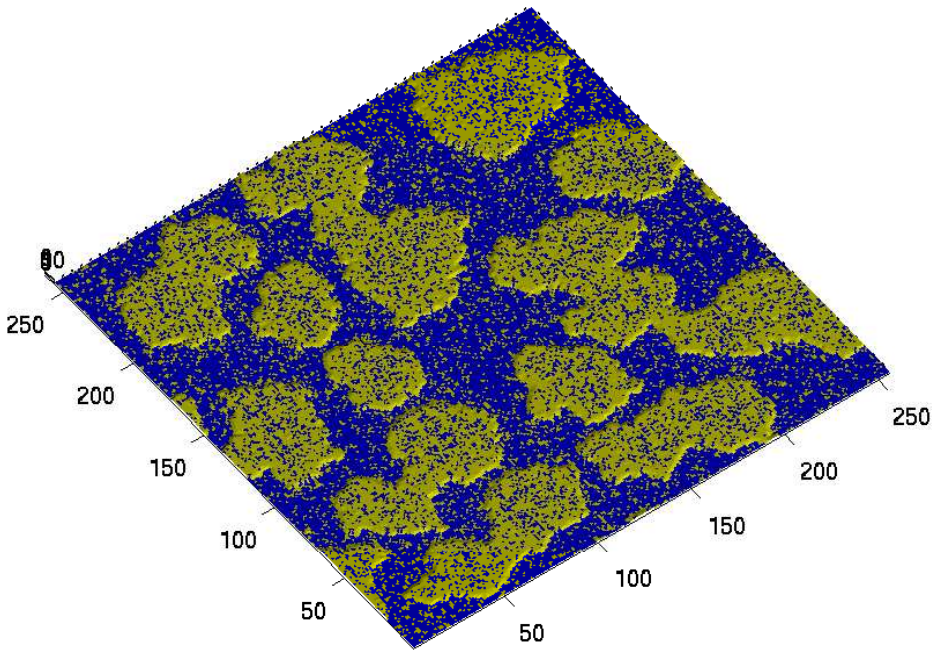

Figure 9: The film is shown after 0.5 monolayers of deposition of yellow colored atoms (Material 2) at T=750 K. At this stage in the growth only two dimensional islands have formed. The presence of blue colored atoms within the two dimensional islands is due to intermixing.

3.4 Summary

The above comparisions indicate that the Surface Decomposition Method gives excellent quantitive agreement with the Local Energy Method with the added feature that it is ten to twenty times faster. This indicates that the approximations used in the Surface Decomposition Method are in fact quite good in a variety of settings. Given this we can now proceed to use this formulation to study various aspects of heteroepitaxial growth.

4 Applications and Implications

In this section we turn to the exploration of the issues outlined in Section 1.1.

4.1 Quantum Dot Alignment

The fact that this new, surface decomposition technique offers significant improvement in speed while at the same time preserving fidelity offers some insight into the importance of various physical processes that take place during heteroepitaxial growth. In particular, it suggests that elastic interactions play a very weak role for low coordinated atoms. This conclusion is significant when one considers what happens during the alignment of stacked quantum dots. In has been suggested

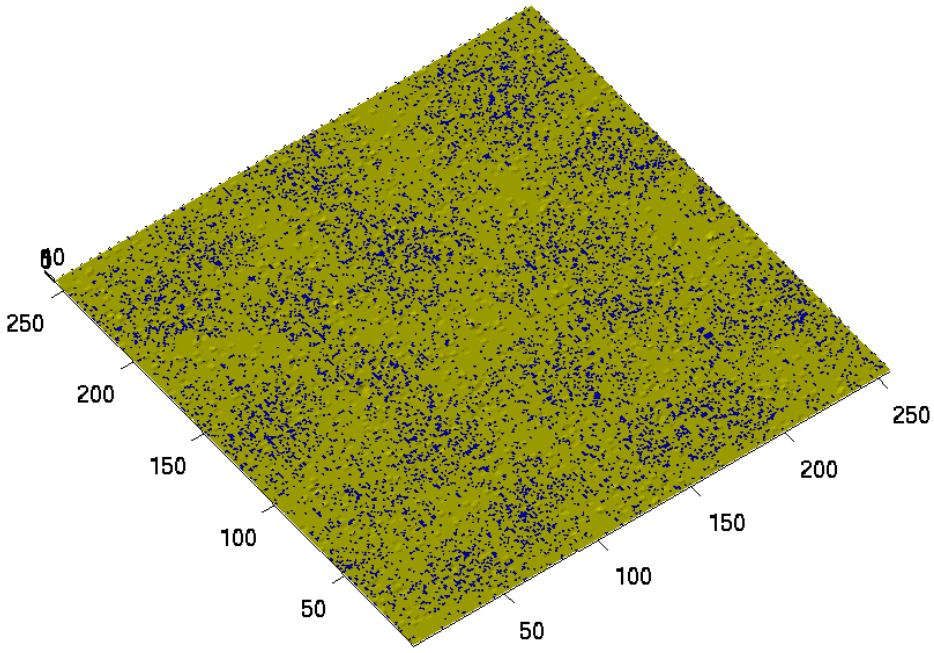

Figure 10: The film is shown after 1.0 monolayers of deposition at T=750 K. Here the two dimensional islands have grown into each other to completely cover the surface. While this single layer of yellow colored atoms is strained, the surface forces prevent the formation of three dimensional islands.

in the literature (e.g. Ref. [38]) that adatoms move to the strained regions of the substrate that are over the buried dots, and, as a consequence, islands will nucleate in these regions. The results here suggest something slightly different happens. Indeed, we observe that islands nucleate essentially at random without regard to the buried dot, and, only when they become big enough, do they start to interact elastically with the buried dots. Before that, the islands were small and dominated by surface forces and entropy. This is demonstrated in Figure 8 which shows results for very small amounts of deposition. For 0.02 ML of deposition, it is evident that the location of the small islands has not yet been influenced by the buried dot. There does seem to be some slight bias at 0.05 ML and by 0.1 ML it is clear that the islands are finally big enough to interact significantly with the buried dot. The discussion above was developed, in part, from conversations with A. Baskaran.

4.2 Parameter Values

Before we present our other series of simulations, we first discuss the issue of parameter values. We will consider a system where the parameters are somewhat close the physical properties of a typical semiconductor material. We are not claiming to simulate a particular system but instead a system whose phenomena are representative of what happens in a variety of actual heteroepitaxial experiments.

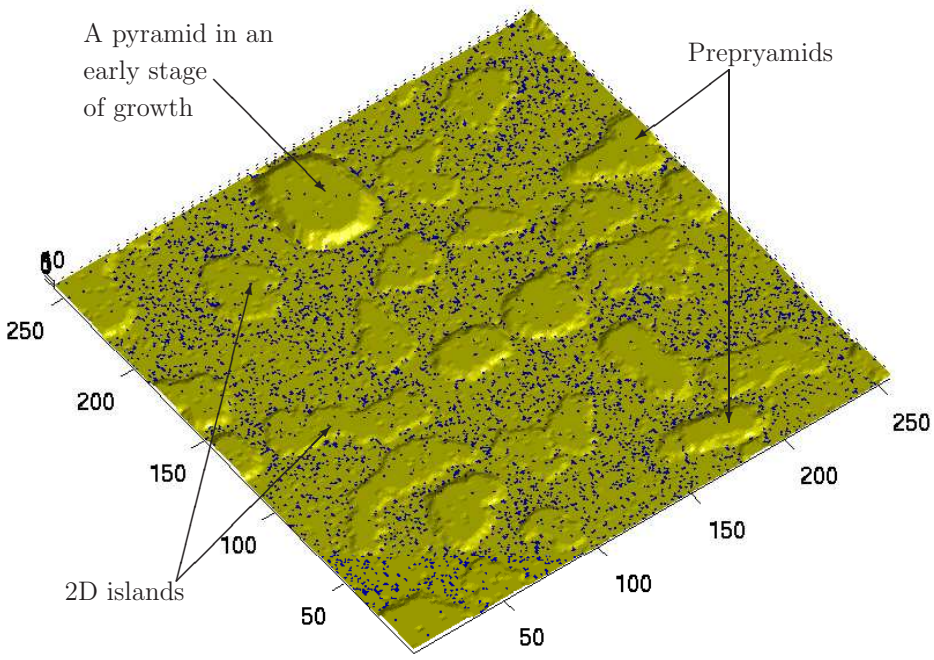

Figure 11: The film is shown after 1.5 monolayers of deposition at T=750 K. At this point in the growth many things have occurred: There are two dimensional islands as would be expected for layer-by-layer growth, several pre-pyramids have formed due to elastic strain, and one of the pre-pryamids has started to form into a fully faceted pyramid.

We again take $a = 0.3$, $b = 0.5$ and $c = 1.0$, but now we choose

$$\gamma_{11} = 0.29\,\text{eV},\ \gamma_{12} = 0.2599\,\text{eV}, \quad \text{and} \quad \gamma_{22} = 0.2510\,\text{eV}.$$

If one takes $\ell = 2.7$Å then, for material 1, the surface energies for the following facets are

$$\sigma_{100} = 2007\,\text{erg/cm}^2, \qquad \sigma_{110} = 1712\,\text{erg/cm}^2 \quad \text{and} \quad \sigma_{111} = 1637\,\text{erg/cm}^2.$$

We have used Eqs. (7-9) to derive these results. These numbers are somewhat close to the surface energies of Silicon. Notice that the surface energies of the (100) interface for material 2 is about 13% smaller than material 1. These choices are fairly close to those reported by Jaccodine [39]. The values for the (100) interface are also close to those chosen by Levine *et al.* [41]. In addition, the (110) and (111) facets have lower energy than the (100) facet, which is also true for Si and Ge.

We note that Mo *et al.* [42] report from experiments that the jumping rate of Si on Si(100) is well approximated by D/ℓ^2 where $D = 10^{-3}\exp(-E_d/kT)\,\text{cm}^2/\text{sec}$ and $E_d \approx 0.67$ eV. This indicates that the hopping rate, assuming a nearest neighbor distance of 2.7 Å, is $1.37\times10^{12}\exp(-E_d/kT)\,\text{sec}^{-1}$. In our simulations we take $E_D = 0.7$ eV and choose the prefactor to be 10^{12}sec^{-1}. This means the energy barrier for the diffusion of an adatom of material 2 on material 1 is 0.7 eV while for material 1 on material 1 it is 0.890 eV and for material 2 on material 2 is 0.640 eV. The diffusion barriers

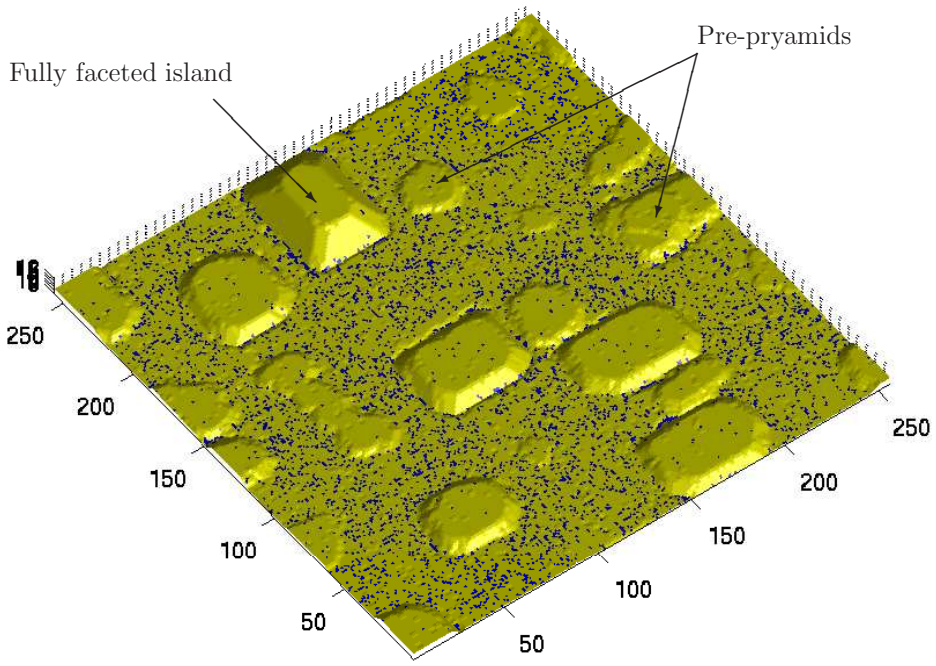

Figure 12: The film is shown after 2 monolayers of deposition at T=750 K. At this stage, most of the two dimensional islands have been consumed by the larger three dimensional islands. There are still several pre-pyramids and one fully faceted three dimensional island.

we are choosing are still slightly too large and this is simply because the code is still somewhat slow. For example, the result shown in Figure 13 took approximately three weeks to generate. If we had used more realistic energy barriers for adatom hopping the simulations would have taken much longer. All our simulations are performed on a single core machine (Intel Xeon 5650, 2.66 GHz).

For the elastic strengths we pick $k_L = 3\,eV/\ell^2$ and $k_D = 10\,eV/\ell^2$. In the continuum limit this gives

$$C_{11} = 23\,\mathrm{eV}/\ell^3 \quad \text{and} \quad C_{12} = C_{44} = 10\,\mathrm{eV}/\ell^3.$$

Now taking $\ell = 2.7$Å and using Eq. (10), we have

$$C_{11} = 18.73 \times 10^{11}\,\mathrm{dynes/cm^2} \quad \text{and} \quad C_{12} = C_{44} = 8.14 \times 10^{11}\,\mathrm{dynes/cm^2}.$$

These are not unreasonable values for a semiconductor. For example, the elastic constants of Silicon [40] are

$$C_{11} = 16.6 \times 10^{11}\,\mathrm{dynes/cm^2}, \quad C_{12} = 6.40 \times 10^{11}\,\mathrm{dynes/cm^2}, \quad \text{and} \quad C_{44} = 7.96 \times 10^{11}\,\mathrm{dynes/cm^2}.$$

For the rest of our simulations we will take $\mu = 0.055$. This value of the misfit is higher than one for Si-Ge, but lower than for GaAs-InAs. We will take $F = 1$ ML/sec and, unless otherwise stated, T =750 K.

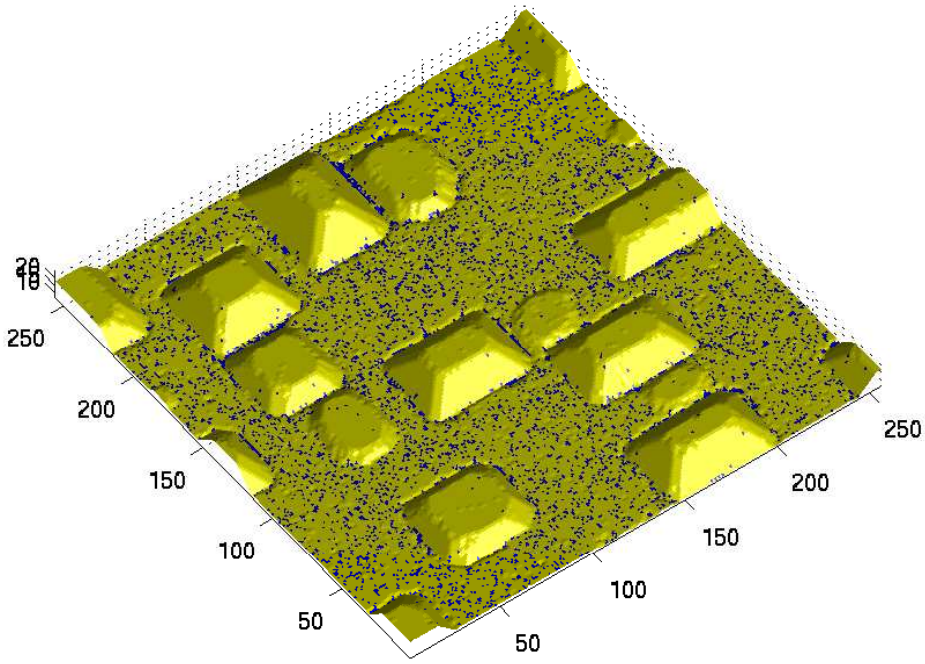

Figure 13: The film is shown after 3 monolayers of deposition at T=750 K. Here most of the film is covered in three dimensional, fully faceted island with a small number of pre-pyramids.

4.3 Stranski-Krastanov Growth

The results of our simulations using the Surface Decomposition Method are displayed in Figures 9 to 13. These simulations shed light on the formation of faceted quantum dots on a faceted surface, what Tersoff *et al.* [43] have referred to as a puzzling phenomenon. Since the quantum dots and the surface are fully faceted, they should be nucleated by a thermally activated process. One might think that the islands would be facetted as soon as they are nucleated, but experiments suggest that instead the faceted quantum dots evolve from pre-pyramids. Recall that pre-prymids are small, multilayer, three dimensional islands whose sides are not faceted.

Figure 9 shows the film after 0.5 ML of deposition, and demonstrates the formation of two-dimensional, i.e. single monolayer, islands. Figure 10 shows that, after 1.0 ML of deposition, the islands have merged to initiate the formation of the wetting layer. Both the two dimensional islands and the wetting layer are strained due to the misfit, but surface energy prevents them from evolving into three-dimensional, i.e. multi-layer, islands.

During the second layer of growth, the surface is now primarily composed of material 2 (yellow colored atoms) so that the surface energy is now lower (see §4.2). This indicates that strain energy is now playing a more important role. Indeed, after 1.5 ML of deposition, see Fig. 11, one starts to see indications of three-dimensional island formation. If one examines Figure 11, one can see three important features: two-dimensional islands, multi-layer islands with irregular boundaries (pre-pyramids), and a single large, three-dimensional island that is in the early stages of becoming

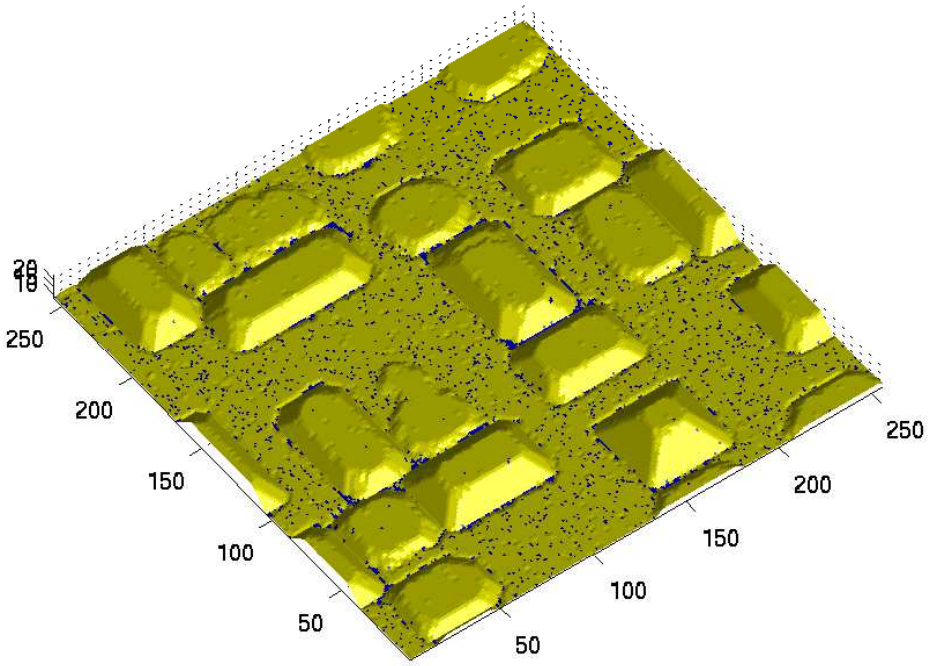

Figure 14: This figure shows the film after 3 monolayers of deposition. The conditions are identical to the results shown in Figures 9 to 13 except the temperature has been lowered to 725 K. The lowering of the temperature reduces atom mobility resulting in more islands that are smaller in size. In addition, the island shapes are more varied, with some rectangular and others square.

faceted. These multilayer islands form one layer at a time. In other words, they nucleate via a layer-by-layer mechanism as discussed in Ref. [31]. We are confident that the pre-pryamids form due to strain relaxation since they do not occur when the misfit is set to zero.

After two monolayers of deposition, one fully facetted three-dimensional island has formed (see, Figure 12). The faceting occurs because the surface energy is anisotropic. There are a number of additional three-dimensional islands in earlier stages of growth, while the two-dimensional islands have largely disappeared, having been incorporated into larger islands.

By three monolayers of growth (Figure 13) the film primarily consists of the fully faceted, three-dimensional islands. It should be pointed out that this morphology is quite stable. Annealing simulations will cause the very small islands to be incorporated into the bigger islands, but the big islands do not appreciably change their size or shape. Similar results were reported in the simulations of Aqua and Frisch [6] and the experiments of Berbezier et al. [50].

In summary, a wetting layer is first formed and then pre-pyramids are created by a layer-by-layer nucleation mechanism that is driven by elastic strain. The pre-pyramids then evolve by surface diffusion into faceted quantum dots. Our results confirm the work of Xiang *et al.* [31] who had predicted that quantum dots would form by a layer-by-layer nucleation mechanism. This indicates that one does not need to resort to the assumption (quoting from Ref. [43]) that "for strained

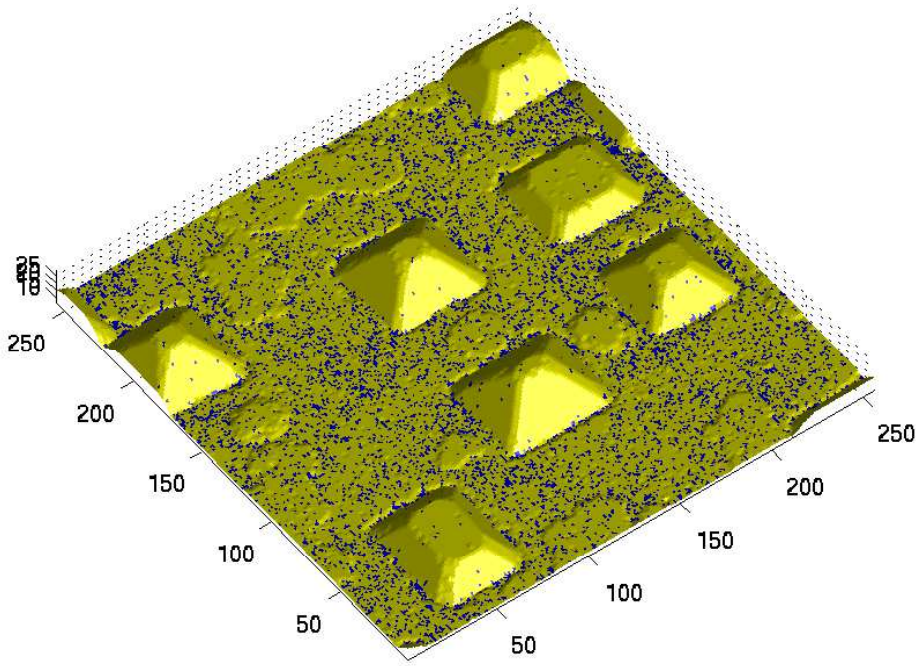

Figure 15: This figure shows the film after 3 monolayers of deposition. The conditions are identical to the results shown in Figures 9 to 13 except the temperature has been raised to 775 K which increases atom mobility resulting in fewer islands that are larger in size. In this case the shapes of the islands are more uniform.

SiGe, the surface-energy anisotropy allows all orientations near (001), with the first facet being (105)" to provide a mechanism for faceted quantum dot formation. This scenario is consistent with experimental results.

The effect of temperature on the morphology is shown in Figures 14 and 15. Comparing Figures 13 and 14, one observes that decreasing the temperature causes the island density to become larger and there are fewer fully facetted quantum dots. On the other hand, comparing Figures 13 and 15, we see that increasing the temperature results in all the quantum dots being facetted with a lower dot density. We attribute these observation to the increased mobility that arises from increasing the temperature. Finally, we show a simulation at a much higher temperature, namely $T = 875$ K. Here we observe an extremely rapid onset of facetted 3D islands. Figure 16 shows that at 1.4 ML no islands have formed and with just an additional 0.2 ML of deposited material a fairly large (13 nm) facetted 3D island has grown as shown on Figure 17.

4.4 Capping

Capping of quantum dots has been widely studied experimentally, for example [44, 45, 46, 47]. It has been established that the quantum dots can erode significantly during capping by a process that is not well understood (e.g. Ref. [44]). In addition it has been observed in some experiments

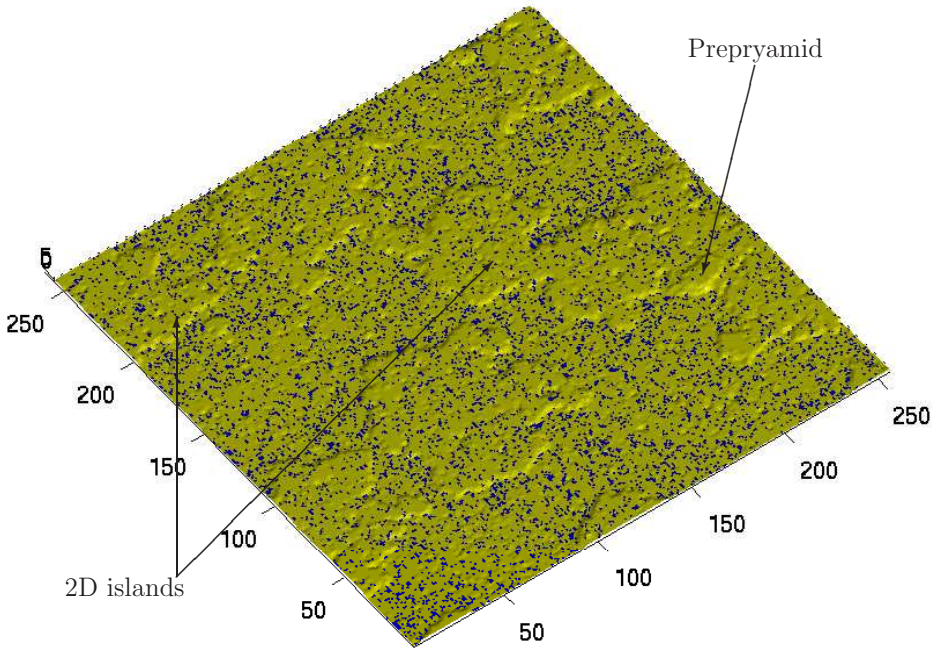

Figure 16: This figure shows the film after 1.4 monolayers of deposition. The conditions are identical to the results shown in Figures 9 to 13 except the temperature has been raised to 875 K. At this point only one small pre-pryamid has formed. The elevated temperature inhibits the formation of pre-pryamids due to entropic effects.

that during capping a fraction of the quantum dots evolve into ring-like structures (e.g. Refs. [45, 46, 47]). Our results not only are able to capture these phenomena, but they also provide insight into the mechanisms behind them.

In our simulations we cap the film shown in Figure 13, which was grown at 750 K, with material 1. We then use a capping temperature of 725 K, selecting this temperature so that a wide range of phenomena would be observed in one realization. If we had picked a much higher temperature, our simulations show that all of the dots will be almost completely eroded; if we had picked a lower temperature, the morphology of the dots would have been unchanged during capping. These observations are consistent with experimental results (e.g. Ref. [44]).

Figure 18 shows the morphology after the quantum dots displayed in Fig. 13 have been capped with 0.6 monolayers of material 1. We observe that the dots have noticeably eroded. Looking at this figure, the mechanism behind this erosion becomes fairly clear. As the capping progresses, the wetting layer becomes more and more covered with material 1 (blue), which has a higher surface energy that material 2 (yellow). This means there is a driving force for the material in the quantum dots to spread onto the wetting layer. A close examination of Figure 18 reveals that the dot material is indeed getting wicked away. Figure 19 presents a cartoon version of this figure to clarify this mechanism. In this way the size of the dots are reduced. This mechanism will be intensified

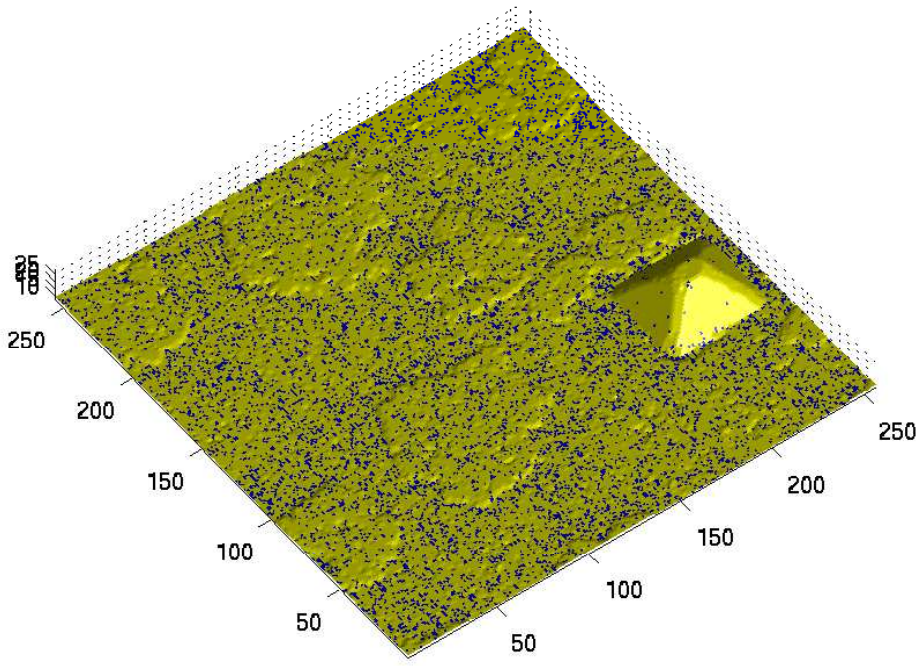

Figure 17: The film is shown after 1.6 monolayers of deposition at T=875 K. This demonstrates the rapid growth of a pre-pryamid into a fully faceted, three dimensional island.

at higher temperatures due to greater mobility. This explains the experimental observation that increasing the temperature will increase dot erosion. It should be remarked that this conclusion is not as obvious as it first sounds, because during the formation of the quantum dots increasing the temperature will enhance dot formation: compare Figures 13, 14 and 15. Finally we point out that Reyes *et al.* [48] have argued that this mechanism is an important feature in liquid drop epitaxy.

Upon further capping, the dots become covered with material 1, and this mechanism is gradually arrested. Further capping results in a situation where many dots have dissolved but several remain. Those that remain are surrounded by what is mainly material 1. Figure 20 shows the film after 4.0 monolayers of capping material have been deposited. There are three quantum dots whose tops are still visible. It is interesting to note that the dot material (yellow colored atoms) is intermixed with the capping material except for a ring-shaped region immediately near the edge of the dot. This behavior has been reported in experiments [49].

These dots are elastically compressed by the material 1 that surrounds them. In many cases it is energetically preferable to relieve this strain energy by ejecting material from the center of the dots, thereby forming ring-like structures. Figure 21 shows an example of this process. Finally, Figure 22 shows a horizontal cross section after all of the dots have been completely capped. This cross section shows that many of the dots originally present have dissolved. Of the four that survived, three evolved into ring-like structures. We have performed simulations over a wide range of parameter values, and we find these ring-like structures to be rather ubiquitous.

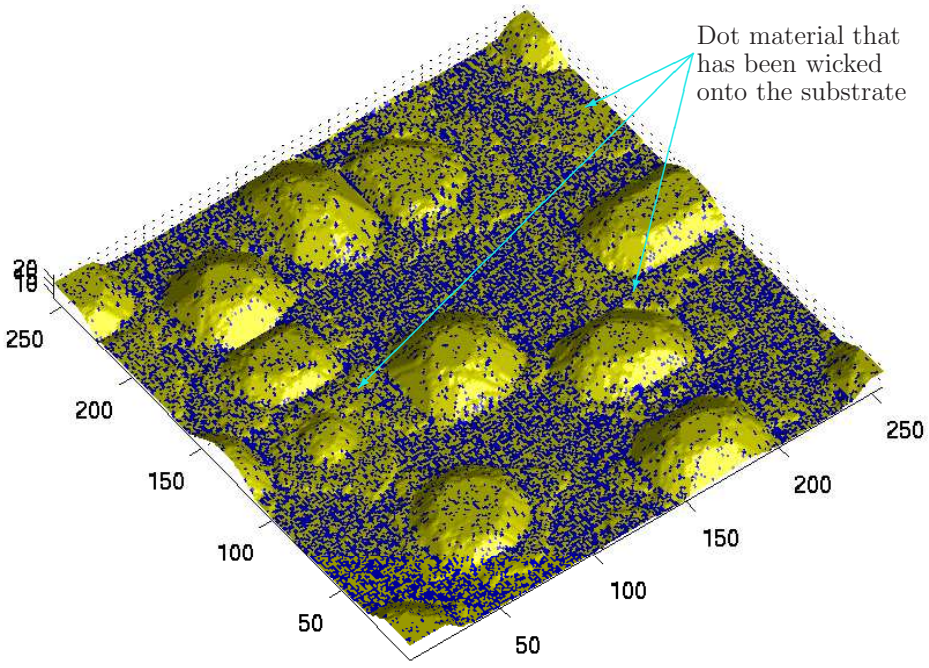

Figure 18: The film shown in Figure 13 is capped with material 1 at T=725 K. This figure shows the result after 0.6 monolayers of capping material (blue colored atoms) have been deposited. The reader should notice that the wetting layer which was primarily compose of material 2 (yellow colored atoms, see, Figure13) now has a high concentration of material 1 (blue colored atoms). This results in a surface with a higher surface energy which in turn provides a driving force for dot material to cover the surface. This figure clearly shows the quantum dots have been reduced in size due to dot material being wicked away to replenish the wetting layer.

In closing, we mention that surface decomposition KMC has recently been applied to study capping of GaAs dots by $Ga_{1-x}In_xAs$ [49]. In that paper the reader will find detailed comparisons of simulations using the algorithm presented here with experimental results.

5 Summary

In this paper we have offered an approximation to a well established KMC model for heteroepitaxial growth. The key to this approximation is that the elastic interaction of low coordinated atoms with the rest of crystal is sufficiently weak that it may be ignored. The resulting model still satisfies detailed balance, and its implementation results in simulation speeds that are close to fifteen times faster. Various tests quantitatively reveal that this approximation is quite faithful to the evolution of the original model. One of these tests implies that the alignment that occurs in the stacking of quantum dots results from interactions between islands and buried dots and not from adatom-buried dot interactions as suggested by other investigations. It is shown that our method can

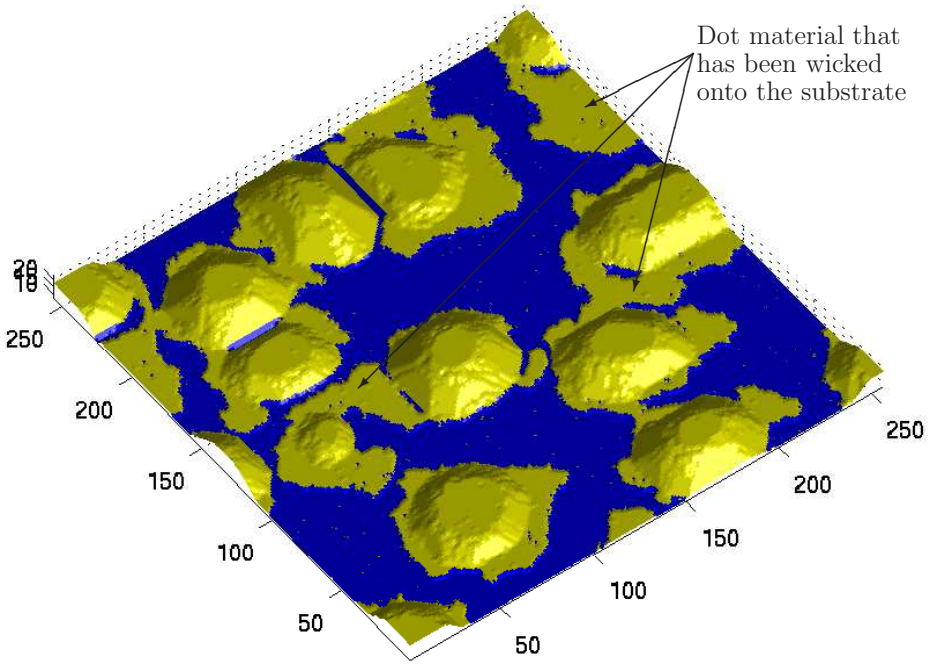

Figure 19: This is a cartoon of Figure 18 that serves to emphasize how the material in the dots is wicked on to the substrate.

simulate Stranski-Krastanov growth. We provide evidence that faceted 3D islands result from the layer-by-layer nucleation of pre-pyramids and fully faceted islands result from anisotropic surface diffusion. The capping of islands is also studied, and it is shown that capping causes erosion of the quantum dots because the dot material is used to replenish the wetting layer. Our simulations are also able to capture the formation of ring-like structures.

Acknowledgments

We thank J.N. Aqua, A. Baskaran, P. Koenraad, J.M. Millunchick, K. Reyes, Y. Saito, and V. Sih, for helpful conversations. This work was supported, in part, by NSF support grants DMS-0810113, DMS-0854870, and DMS-1115252.

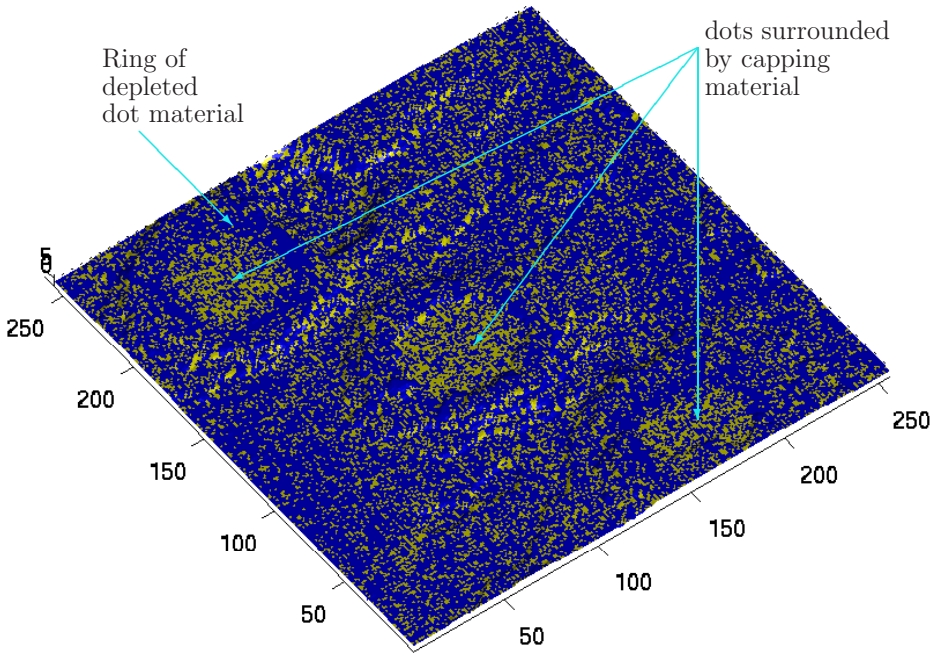

Figure 20: This shows the result after 4 ML of capping at T=725 K. This figure shows three dots that have been completely surrounded by capping material. The surrounded dots are now being compressed by the capping material which greatly increases their elastic energy.

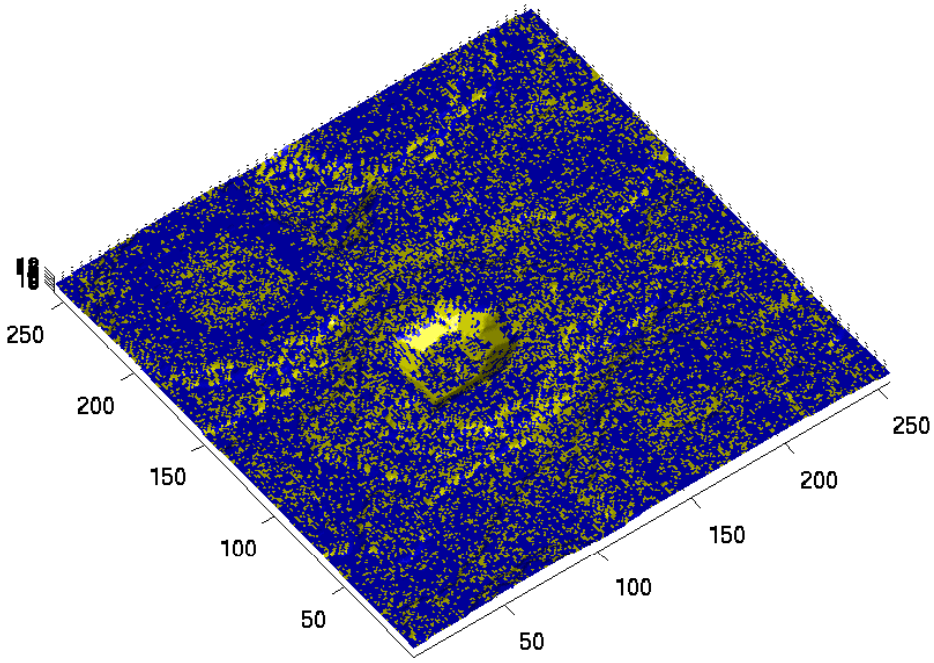

Figure 21: This shows the result after 4.5 ML of capping at T=725 K. The high strain energy inside the dots provides a driving force for material to leave. If the dot material can leave before it has been covered by the capping material a crater will form. This figure shows the formation of a crater in which most of the dot material has left, leaving behind a small ring of material 2 (yellow colored atoms). Further deposition results in the crater being filled with capping material. The small ring appears to be fairly undisturbed by the subsequent capping process, resulting in a nanoring.

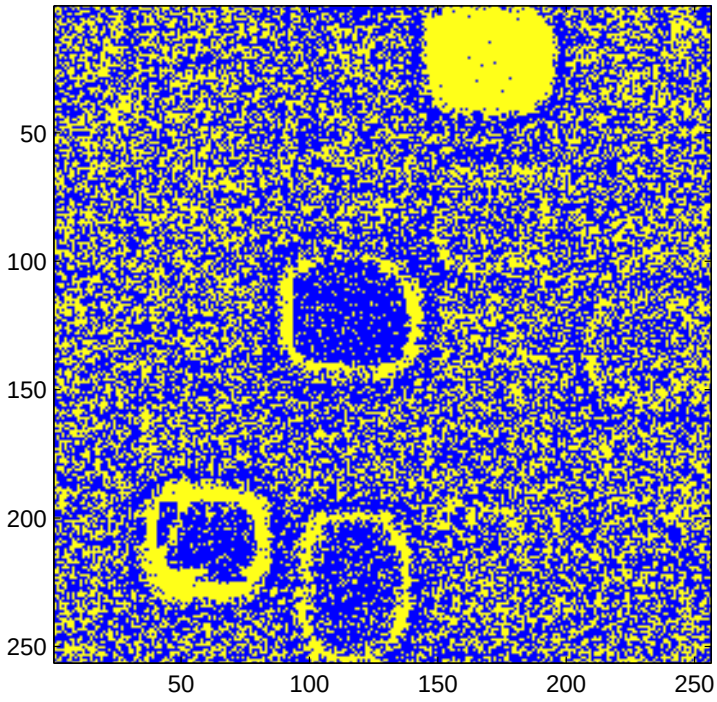

Figure 22: A horizontal cross section of the film is presented after 8 ML of capping. This slice is located 2 ML above the the substrate. This figure shows that 3 nanorings have formed. In addition it shows that one of the dots managed to survive the capping process.

References

[1] X. Niu, R. Vardavas, R.E. Caflisch, and C. Ratsch, *Phys. Rev. B* **74**, Art. No. 193403 (2006).

[2] X. Niu, Y.L. Lee, R.E. Caflisch, and C. Ratsch, *Phys. Rev. Lett.* **101**, Art. No. 086103 (2008).

[3] C. Ratsch, J. Devita, and P. Smereka, *Phys. Rev. B* **80**, Art. No. 155309 (2009).

[4] Wise, S.M., Lowengrub, J.S., Kim, J.S., Johnson, W.C., *Superlattices Microstruct.* **36**, 293304 (2004).

[5] Wise, S.M., Lowengrub, J.S., Kim, J.S., Thornton, K., Voorhees, P.W., Johnson, W.C., **Appl. Phys. Lett. 87**, Art. No. 133102 (2005).

[6] J.N. Aqua and T. Frisch, *Phys. Rev. B* **82** 2555 (2010).

[7] M. Ortiz, E.A. Repetto, and H. Si, *J. Mech. Phys. Sol.* **47**, 697-730 (1999).

[8] B.J. Spencer, P.W. Voorhees, and S.H. Davis, *Phys. Rev. Lett.* **67**, 3696-3699 (1991).

[9] Y. Tu and J. Tersoff, *Phys. Rev. Lett.* **93** 216101 (2004).

[10] C.H. Lam, C.K. Lee, and L.M. Sander, *Phys. Rev. Lett.* **89**, 16102 (1-4) (2002).

[11] Lee S., Caflsich R.E., Lee Y.J. *SIAM J. Appl. Math.* **66**, 17491775 (2006).

[12] M.T. Lung, C.H. Lam, and L.M. Sander, *Phys. Rev. Lett.* **95** Art. No. 086102 (2005).

[13] G. Russo and P. Smereka, *J. Comput. Phys.* **214**, 809-828 (2006).

[14] G. Russo and P. Smereka, *Multiscale Model. Simu.* **5**, 130-148 (2006).

[15] T.P. Schulze and P.Smereka, *J. Mech. Phys. Solids.* **57** 521-538 (2009).

[16] T.P. Schulze and P. Smereka, *Comm. Comput. Phys.* **10** 1089-1112 (2011).

[17] D. Leonard, K. Pond, and L.M. Petroff, *Phys. Rev. B* **50** 11687-11692 (1994).

[18] R.J. Asaro and W.A. Tiller, *Metall. Trans.* **3** 1789 (1972).

[19] M.A. Grinfeld, *J. Nonlinear Sci.* **3** 35 (1993).

[20] J. Tersoff, *Phys. Rev. B* **43**, 9377-9380 (1991).

[21] A. Baskaran and P. Smereka, J. Appl. Phys. **111** Art. No. 044321 (2012).

[22] A. Baskaran, J. Devita, and P. Smereka, *Contin. Mech. Thermo.* **22** 1-26 (2010).

[23] C.H. Lam, *J. Applied Physics* **108**, Art. No. 064328, (2010).

[24] C.H. Lam, *Physical Review E* **81**, Art. No. 021607, (2010).

[25] B.G. Orr, D.A. Kessler, C.W. Snyder, and L.M. Sander, *Europhysics Lett.* **19**, 33-38 (1992).

[26] L.M. Sander, Advanced Condensed Matter Physics, Cambridge University Press, Cambridge (2009). (see page 61).

[27] C. Rottman and M. Wortis, *Phys. Rev. B* **24**, 6274-6277 (1981).

[28] J.P. Devita, L.M. Sander, and P. Smereka, Phys. Rev. B **72**, Art. No. 205421 (2005).

[29] C. Rottman and M. Wortis, *Phys. Rev. B* **29**, 328-339 (1984).

[30] H.J. Leamy, G.H. Gilmer, and K.A. Jackson, Statistical Thermodynamics of Clean Surfaces, in Surface Physics of Material vol. 1, ed J.M. Blakely, Academic Press, New York 1975.

[31] R.X. Xiang, M.T. Lung, C.H. Lam, *Physical Review E* **82**, Art. No. 021602 (2010).

[32] W.K. Burton, N. Cabrera, and F.C. Frank, *Trans. R. Soc. London Ser. A* **243**, 299 (1951).

[33] T.P. Schulze, P. Smereka and W. E, to Epitaxial Growth, *J. Comp. Phys.* **189** 197-211 (2003).

[34] I.V. Markov, Crystal growth for Beginners: Fundamentals of Nucleation, Crystal Growth, and Epitaxy, World Scientific (2003).

[35] M. Biehl, M. Ahr, W. Kinzel, and F. Much, *Thin Solid Films* **428**, 52-55 (2003).

[36] W. Guo, T.P. Schulze and W. E, Simulation of Impurity Diffusion in a Strained Nanowire Using Off-lattice KMC, *Comm. Comp. Phys.* **2** 164-176 (2007).

[37] J.L. Blue, I. Biechl, and F. Sullivan, *Phys. Rev. E* **51** 876 (1995).

[38] J. Tersoff, C. Teichert, and M.G. Lagally, *Phys. Rev. Lett.* **76** 1675-1678 (1996).

[39] R.J. Jaccodine, *J. Electrochemical Soc.* **110** 524-527 (1963).

[40] Electronic Archive, Ioffe Physico-Technical Institute, `http://www.ioffe.ru/SVA/NSM/Semicond/Si/mechanic.html`

[41] M.S. Levine, A.A. Golovin, S.H. Davis, and P.W. Voorhees, *Phys. Rev. B* **75** Art. No. 205312 (2007).

[42] Y.W. Mo, J. Kleiner, M.B. Webb, and M.G. Lagally, *Phys. Rev. Lett.* **66**, 1998-2001 (1991).

[43] J. Tersoff. B.J. Spencer, A. Rastelli, H. von Känel, *Phys. Rev. Lett.* **89**, Art. No. 196104, (2002).

[44] Q. Gong, P. Offermans, R. Nötzel, P.M. Koenraad, and J.H. Wolter, *Appl. Phys. Lett.* **85** 5697-5699 (2004).

[45] J. M. Garcia, G. Medeiros-Ribeiro, K. Schmidt, T. Ngo, J.L. Feng, A. Lorke, J. Kotthaus, and P. M. Petroff, *Appl. Phys. Lett.* **71**, 2015-2017 (1997).

[46] R. Timm, H. Eisele, A. Lenz, L. Ivanova, G. Balakrishnan, D.L. Huffaker, and M. Dähne, *Phys. Rev. Lett.* **101**, Art. No. 256101, (2008).

[47] P. Offermans, P. M. Koenraad, J. H. Wolter D. Granados, J. M. Garca, V. M. Fomin, V.N. Gladilin, and J.T. Devreese, *Appl. Phys. Lett.* **87** Art. No. 131902 (2005).

[48] K. Reyes, P. Smereka, D. Nothern, J.M. Millunchick, C. Somaschini, S. Bietti, C. Frigeri, and S. Sanguinetti, in preparation.

[49] J.G. Keizer, P.M. Koenraad, P. Smereka, J.M. Ulloa, A. Guzman, and A. Hierro, *Phys. Rev. B* **85**, art. no. 155326 (2012).

[50] I. Berbezier, A. Ronda, F. Volpi, and A. Portavoce, *Surf. Sci.* **531**, 231 (2003).